



Plane-strain deformation of an elastic material compressed in a rough rectangular cavity

A. Warlock^a, H.-K. Ching^b, A.K. Kapila^{a,*}, R.C. Batra^b

^a *Department of Mathematical Sciences, Rensselaer Polytechnic Institute, Troy, NY 12180, USA*

^b *Department of Engineering Science and Mechanics, MC 0219, Virginia Polytechnic Institute and State University, Blacksburg, VA 24061, USA*

Received 27 June 2001; received in revised form 8 September 2001; accepted 5 October 2001

(Communicated by I. STAKGOLD)

Abstract

Deformation and stress distributions in a linear elastic solid, confined to a rigid cavity with rough walls and subjected to uniform compression from one end, are examined. Wall roughness is modeled by Coulomb friction. At the rigid walls, one boundary condition involves deformation and the other stresses, and this renders the problem non-standard. A Laplace transformation solution is constructed for a semi-infinite cavity, and a computational solution for a cavity with finite length. Agreement between the two solutions is good, and improves with increasing cavity lengths and higher coefficients of friction. There exists a critical value of the coefficient of friction below which the axial displacements decay monotonically with distance from the loaded end and the material points stay in contact with the rough walls. For supercritical values of the coefficient of friction, displacements and stresses on the rough walls exhibit oscillatory behavior in the axial direction. The material loses contact with the walls, and the analytical solution presented here loses validity. © 2002 Elsevier Science Ltd. All rights reserved.

Keywords: Coulomb friction; Corner singularities; Analytical solution; Numerical solution

1. Introduction

Our interest in the problem under study stems from our recent treatment of a related but different problem, namely, the consolidation of a non-cohesive powder via compaction [1,2]. Uniaxial pressing is a common technological process in which solid grains are placed in a

* Corresponding author. Tel.: +1-518-276-6894; fax: +1-518-276-4824.
E-mail address: kapila@rpi.edu (A.K. Kapila).

cylindrical die into which two pistons are inserted. One of the pistons is generally held stationary while the other is pushed in to compact the powder. The compaction process is generally quite slow, and the major goal is to produce a specimen in which density distribution is as close to uniform as possible. Experimental data on explosive pressing [3] show that when a one-inch long cylindrical specimen of powdered explosive is pressed in a one-inch diameter tube of polished steel, statically, only 60% of the load applied at one face of the specimen is transmitted to the other face, the remaining 40% being supported by friction at the walls. A rather different application of compaction occurs in the so-called DDT (deflagration-to-detonation transition) tube tests on high-energy explosives [4]. The test apparatus consists of a sealed tube completely filled with lightly tamped explosive powder. The explosive is subjected to mechanical stimulus at one end of the tube by a moving piston. The piston drives a shock-like wave of compaction through the explosive bed, increasing the solid volume fraction from 70–75% to 90–95% and initiating ignition. Friction plays a role in this dynamic problem as well, the details of which were examined in recent studies of a rather simple fluid-like model of the powder, with the assumption of Coulomb friction at the walls [1,2]. It was found, as expected, that friction causes the pressure at the piston face to rise with time if the piston is driven at a constant speed, and the speed of the piston to drop if the piston is driven at a constant pressure, with concomitant effects on the strength of the compaction shock and on the distribution of the state between the shock and the piston. We found, in particular, that for small values of the coefficient of friction the decay from the piston to the shock was monotonic, but at higher values oscillations crept in. The desire to discover whether a similar non-monotonicity of deformation is exhibited by an elastic material at higher coefficients of friction led to the present study.

We consider only the static deformation of the material as it is compressed in a planar, rectangular, rigid cavity whose walls are rough. Under the assumption of plane strain, powerful analytical techniques based on the theories of complex variables and singular integral equations are available for construction of the solution [5]. What makes the problem non-standard, and the application of these techniques difficult, is the pair of boundary conditions on the rough wall, where rigidity leads to a condition on displacements and roughness to a condition on stresses. Expansion in terms of the eigenfunctions of the biharmonic equation is another possible approach, but questions of completeness and orthogonality for the boundary conditions at hand again lead to complexity. We opt for the Laplace transformation, which has the advantage that completeness and orthogonality are dealt with automatically, and the limitation that it only applies to a semi-infinite domain. However, the friction-induced decay suggests that results for the unbounded configuration may well provide a good approximation for those for the finite configuration. A comparison of the analytical results against those obtained numerically for a finite domain confirms that accuracy of the approximation is indeed good, and improves with increase in the coefficient of friction or the length of the cavity.

The paper begins by giving the formulation of the problem in Section 2. Section 3 gives an analytical solution of the problem by the Laplace transform method following a discussion of corner singularities. A weak formulation of the problem suitable for seeking a numerical solution by the meshless local Petrov–Galerkin method is given in Section 4. The deformation and the stress fields computed by the two methods are compared in Section 5. Effects on the deformation and stress distributions of varying the friction coefficient are examined. We find that for friction coefficients above a critical value oscillations appear, and necessitate a reconsideration of the Coulomb model.

2. Formulation of the problem

A schematic sketch of the configuration is shown in Fig. 1. We use rectangular Cartesian coordinates to describe static deformations of the linear elastic material compressed in the rigid cavity with rough horizontal walls at $x_2 = \pm 1$ and smooth rigid vertical walls at $x_1 = 0$ and L . We presume that a plane-strain state of deformation prevails; thus the dimension in the x_3 -direction is very large as compared to 2 and L . In the absence of body forces, equations governing the deformations of the body are

$$\sigma_{ij,j} = 0, \quad i, j = 1, 2, \tag{2.1}$$

$$\sigma_{ij} = \lambda e_{kk} \delta_{ij} + 2\mu e_{ij}, \tag{2.2}$$

$$e_{ij} = (u_{i,j} + u_{j,i})/2, \tag{2.3}$$

$$u_1(L, x_2) = 0, \quad \sigma_{21}(L, x_2) = 0, \quad -1 \leq x_2 \leq 1, \tag{2.4a}$$

$$u_1(0, x_2) = u_0, \quad \sigma_{21}(0, x_2) = 0, \quad -1 \leq x_2 \leq 1, \tag{2.4b}$$

and for $0 < x_1 < L$,

$$u_2(x_1, \pm 1) = 0, \tag{2.4c_1}$$

and either

$$u_1(x_1, \pm 1) = 0 \quad \text{if } \sigma_{12}(x_1, \pm 1) < \mu_f |\sigma_{22}(x_1, \pm 1)| \quad \text{and} \quad \sigma_{22}(x_1, \pm 1) < 0, \tag{2.4c_2}$$

or

$$\sigma_{12}(x_1, \pm 1) = -\mu_f |\sigma_{22}(x_1, \pm 1)| \frac{u_1(x_1, \pm 1)}{|u_1(x_1, \pm 1)|}, \quad \sigma_{22}(x_1, \pm 1) < 0, \tag{2.4c_3}$$

or

$$\sigma_{12}(x_1, \pm 1) = 0, \quad \sigma_{22}(x_1, \pm 1) \geq 0. \tag{2.4c_4}$$

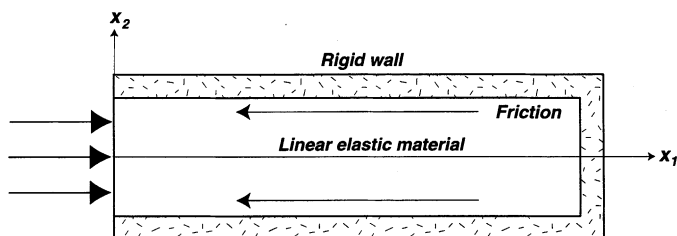


Fig. 1. A rectangular rigid cavity enclosing a linear elastic material.

Here σ is the stress tensor, \mathbf{e} the infinitesimal strain tensor, \mathbf{u} the displacement of a point, a comma followed by the index j indicates partial differentiation with respect to x_j , a repeated index implies summation over the range of the index, λ and μ are the Lamé constants, and μ_f is the coefficient of friction between the walls of the cavity and the deformable material. The boundary conditions (2.4a)–(2.4c₄) imply that a material point of the deformable body cannot penetrate through the rigid walls of the cavity. At the surfaces of the upper and lower rough walls, a material point of the deformable body can slide over the wall only if the tangential traction is sufficient to overcome the frictional force. Also, a material point may separate away from the wall in which case it is on a free surface. These three possibilities are listed in Eqs. (2.4c₂)–(2.4c₄), and make the problem quite challenging. Substitution from (2.3) into (2.2) and the result into (2.1) gives a set of second-order, linear, coupled partial differential equations (2.5) for the determination of the two components of the displacement \mathbf{u} :

$$(\lambda + \mu)u_{k,ki} + \mu u_{i,jj} = 0. \quad (2.5)$$

In the absence of friction the problem has the following simple solution:

$$u_1(x_1, x_2) = u_0 \left(1 - \frac{x_1}{L}\right), \quad u_2(x_1, x_2) = 0. \quad (2.6)$$

However, in the presence of friction, it is not easy to find an analytical solution of the problem, especially for finite values of L . Here we study in detail the case when the boundary condition (2.4c₃) holds and delimits the values of μ_f for which the solution is valid. In view of the axial displacements prescribed on the left end, we anticipate that the boundary condition (2.4c₃) applies; it will be verified a posteriori. We first give an analytical solution of the problem for $L = \infty$, and then a numerical solution of the problem for finite values of L . It is found that the numerical solution of the problem agrees well with the analytical solution except at points very close to the smooth, rigid, right wall. The rate of decay of the solution in the axial direction varies with the value assigned to the coefficient of friction. Thus the correlation between the analytical solution for $L = \infty$ and the numerical solution for a finite value of L depends also upon the coefficient of friction.

3. Analytical solution for the semi-infinite cavity

It is anticipated that the solution of the problem for the semi-infinite cavity will provide a substantial amount of information about the behavior of the solution for the finite-strip. For the former geometry the boundary conditions (2.4a) are replaced by

$$\lim_{x_1 \rightarrow \infty} u_1(x_1, x_2) = 0, \quad \lim_{x_1 \rightarrow \infty} \sigma_{21}(x_1, x_2) = 0, \quad |x_2| < 1. \quad (3.1)$$

By introducing the Airy stress function, the problem can of course be recast as a boundary-value problem for the biharmonic equation. In this formulation the semi-infinite elastostatic strip has attracted considerable attention, the primary emphasis having been on the construction of Fourier-series solutions in terms of the so-called Papkovitch–Fadle eigenfunctions. Thus,

algorithms have been derived for the computation of the Fourier coefficients [6,7], the question of completeness of eigenfunctions has been addressed and conditions stated for the convergence of the series [8–10], and the role played by possible corner singularities has been elucidated [11]. All of this work assumes stress-free boundary conditions on the walls, and is therefore not directly applicable to the present situation.

The problem can be solved by using the Laplace transformation in x_1 if the functions involved are Laplace transformable, and u_1 , $u_{1,1}$, u_2 and $u_{2,1}$ at $x_1 = 0$ are known. The first and the fourth of these quantities are given as boundary data. The other two are unknown but will be assumed to possess Fourier series in x_2 , with the coefficients of the series determined as a part of the solution. Since u_i and $u_{i,j}$ are expected to be bounded within the body and to vanish at infinity, the only sources of difficulty in taking the Laplace transform are the possible singularities in $u_{i,j}$ at the corners $(0, \pm 1)$. For example, if $u_{1,1}(0, x_2)$ is unbounded as $x_2 \rightarrow \pm 1$, then its singular behavior will need to be subtracted out before it can be Fourier expanded for taking its Laplace transform (e.g., see [12]). Such singularities are admissible since stresses and hence displacement gradients are only required to be integrable rather than bounded at the boundaries. We use similarity analysis at the corners to identify the potential singularities there.

3.1. Corner solutions

In order to characterize the likely singularities in the solution at the corner $(0, 1)$, we introduce a polar coordinate system with the origin at $(0, 1)$. The coordinates of a point in the two coordinate systems are related as $x_2 - 1 = r \sin \theta$, $x_1 = r \cos \theta$, with $-\pi/2 < \theta < 0$. Note that the form of the singularity as $r \rightarrow 0$ should be independent of θ ; thus we look for a product solution.

By eliminating $u_2(u_1)$ from the two partial differential equations (2.5) we obtain $\nabla^4 u_1 = 0$ ($\nabla^4 u_2 = 0$). Thus both u_1 and u_2 are biharmonic. However, not all biharmonic functions satisfy (2.5). Biharmonic functions of the product form that give bounded values of the displacement \mathbf{u} but singular behavior of $\nabla \mathbf{u}$ as $r \rightarrow 0$ are of the following two types:

1. $r(c_0 \sin \theta + c_1 \theta \sin \theta + c_2 \cos \theta + c_3 \theta \cos \theta) + r \ln r(d_0 \sin \theta + d_1 \theta \sin \theta + d_2 \cos \theta + d_3 \theta \cos \theta)$,
 2. $r^b(g_0 \sin(b\theta) + g_1 \sin((2-b)\theta) + g_2 \cos(b\theta) + g_3 \cos((2-b)\theta))$.
- (3.2)

Here $c_0, c_1, c_2, c_3, d_0, d_1, d_2, d_3, g_0, g_1, g_2, g_3$ and b are constants. Warlock [2] has shown that there are no solutions of the type (3.2) that give bounded values of \mathbf{u} but unbounded values of $|\nabla \mathbf{u}|$ at the corners $(0, \pm 1)$. However, there could be solutions with $|\nabla \nabla \mathbf{u}|$ unbounded.

3.2. The Laplace-transform solution

Due to the symmetry of the problem about the horizontal centroidal axis, u_2 is an odd and $u_{1,1}$ an even function of x_2 . Thus at the edge $x_1 = 0$, these can be assumed to have the forms

$$u_{1,1}(0, x_2) = a_0 + \sum_{n=1}^{\infty} a_n \cos(n\pi x_2), \quad (3.3a)$$

$$u_2(0, x_2) = \sum_{n=1}^{\infty} b_n \sin(n\pi x_2). \quad (3.3b)$$

We apply the Laplace transform

$$U_i(p, x_2) = \int_0^{\infty} e^{-px_1} u_i(x_1, x_2) dx_1, \quad i = 1, 2, \quad (3.4)$$

to Eq. (2.5) and the boundary conditions (2.4a)–(2.4c₄), and obtain

$$(1 - 2\nu)U_1'' + 2p^2(1 - \nu)U_1 + pU_2' \\ = \sum_{n=1}^{\infty} n\pi b_n \cos(n\pi x_2) + 2(1 - \nu) \left(pu_0 + a_0 + \sum_{n=1}^{\infty} a_n \cos(n\pi x_2) \right), \quad (3.5a)$$

$$2(1 - \nu)U_2'' + (1 - 2\nu)p^2U_2 + pU_1' = (1 - 2\nu)p \sum_{n=1}^{\infty} b_n \sin(n\pi x_2), \quad (3.5b)$$

$$U_2(p, 1) = 0, \quad (3.6a)$$

$$U_2(p, -1) = 0, \quad (3.6b)$$

$$(1 - 2\nu)U_1' - 2\mu_f \nu p U_1 - 2\mu_f(1 - \nu)U_2' = -2\mu_f \nu u_0 \quad \text{at } x_2 = 1, \quad (3.6c)$$

$$(1 - 2\nu)U_1' + 2\mu_f \nu p U_1 + 2\mu_f(1 - \nu)U_2' = 2\mu_f \nu u_0 \quad \text{at } x_2 = -1. \quad (3.6d)$$

Here a prime indicates derivative with respect to x_2 , and $\nu = \lambda/(2(\lambda + \mu))$ is the Poisson ratio. The far field condition (3.1) imposes two restrictions on U_1 . Curbing of exponential growth demands that there be no poles in the right-half plane, and the avoidance of algebraic growth requires that

$$\lim_{p \rightarrow 0} pU_1 = 0. \quad (3.7)$$

Eqs. (3.5a) and (3.5b) are a system of linear ordinary differential equations. We write these as a first-order system of four equations in four unknowns: U_1 , U_2 , U_1' , U_2' . We first find a homogeneous solution of these equations and then a particular solution by the method of undetermined coefficients. A general solution is

$$U_1 = A \sin(px_2) + B \cos(px_2) + Cx_2 \sin(px_2) + Dx_2 \cos(px_2) + \frac{a_0}{p} + \frac{u_0}{p} + \sum_{n=1}^{\infty} A_n \cos(n\pi x_2), \quad (3.8a)$$

$$U_2 = A \cos(px_2) - B \sin(px_2) + Cx_2 \cos(px_2) - C \frac{3 - 4\nu}{p} \sin(px_2) - Dx_2 \sin(px_2) - D \frac{3 - 4\nu}{p} \cos(px_2) + \sum_{n=1}^{\infty} B_n \sin(n\pi x_2), \tag{3.8b}$$

where A, B, C, D are constants of integration, and

$$A_n = \frac{((1 - 2\nu)p^2 - 2(1 - \nu)(n\pi)^2)a_n - (n\pi)^3 b_n}{(1 - 2\nu)(p - n\pi)^2(p + n\pi)^2}, \tag{3.9a}$$

$$B_n = \frac{p((1 - 2\nu)p^2 + 2(n\pi)^2\nu)b_n + pn\pi a_n}{(1 - 2\nu)(p - n\pi)^2(p + n\pi)^2}. \tag{3.9b}$$

Substitution from (3.8a) and (3.8b) into the boundary conditions (3.6a)–(3.6d) gives four equations for the determination of A, B, C and D . Their solution gives

$$A = 0, \quad B = \frac{(p \cos p - (3 - 4\nu) \sin p)}{2(1 - 2\nu)p h(p)} J(p), \tag{3.10a}$$

$$D = 0, \quad C = \frac{\sin p}{2(1 - 2\nu)p h(p)} J(p), \tag{3.10b}$$

where

$$J(p) = \frac{2\mu_f \nu}{p} a_0 + \sum_{n=1}^{\infty} \frac{(-1)^n 2\mu_f p}{(p^2 - n^2\pi^2)^2} (\nu p^2 + n^2\pi^2(1 - \nu)) a_n + \sum_{n=1}^{\infty} \frac{(-1)^n 2\mu_f pn\pi}{(p^2 - n^2\pi^2)^2} ((1 - \nu)p^2 + \nu n^2\pi^2) b_n, \tag{3.11a}$$

$$h(p) = \mu_f p + 2(1 - \nu) \sin^2 p - (1 - 2\nu)\mu_f \sin p \cos p. \tag{3.11b}$$

The coefficients a_n and b_n in Eq. (3.3a) and (3.3b) are determined by requiring that the solution decay at infinity. Upon expanding various terms in the expression (3.8a) for U_1 in Taylor series about $p = 0$, and using the condition (3.7), we obtain

$$\frac{(1 - \nu)a_0}{\mu_f \nu} + u_0 = 0. \tag{3.12}$$

Curbing exponential growth at infinity requires the absence of singularities in the transformed solution in the right-half plane. Thus we must set to zero the residues of any apparent poles there. There are two sets of apparent poles: $p_n = n\pi$, and the roots p_k of $h(p_k) = 0$ with positive real parts. Straightforward algebraic calculations show that these requirements lead to

$$J(p_k) = 0. \tag{3.13}$$

Values of a_0, a_1, a_2, \dots and b_1, b_2, \dots are found by solving Eqs. (3.12) and (3.13).

3.3. Inverting the Laplace transform

We obtain displacements $u_i(x_1, x_2)$ by taking the inverse transforms of $U_i(x_1, x_2)$, i.e.,

$$u_i(x_1, x_2) = \frac{1}{2\pi i} \int_{\gamma-i\infty}^{\gamma+i\infty} e^{px_1} U_i(p, x_2) dp, \tag{3.14}$$

where $\gamma > 0$. There are no branch points, and completion of contour in the left-half plane in the usual way yields

$$u_1(x_1, x_2) = \sum_{p_k} e^{p_k x_1} \frac{\bar{B}(p_k, x_2) J(p_k)}{2(1 - 2\nu) p_k (\partial h(p_k) / \partial p_k)}, \tag{3.15a}$$

$$u_2(x_1, x_2) = \sum_{p_k} e^{p_k x_1} \frac{\bar{C}(p_k, x_2) J(p_k)}{2(1 - 2\nu) p_k (\partial h(p_k) / \partial p_k)}, \tag{3.15b}$$

where the p_k are the roots of $h(p) = 0$ with negative real parts, and

$$\bar{B}(p, x_2) = (p \cos p - (3 - 4\nu) \sin p) \cos(px_2) + px_2 \sin p \sin(px_2),$$

$$\bar{C}(p, x_2) = px_2 \sin p \cos(px_2) - p \cos p \sin(px_2).$$

4. Numerical solution of the problem

We use the meshless local Petrov–Galerkin (MLPG) method to find a numerical solution of the problem defined by Eqs. (2.1)–(2.4c₄). We first derive the local symmetric weak form.

Let Ω denote the rectangular region $[0, L] \times [-1, 1]$ shown in Fig. 1 and occupied by the linear elastic body, and $\Gamma = \partial\Omega$. We write the boundary conditions (2.4a)–(2.4c₄) as

$$u_i = \bar{u}_i \quad \text{on } \Gamma, \tag{4.1a}$$

$$t_i \equiv \sigma_{ij} n_j = \bar{t}_i \quad \text{on } \Gamma, \tag{4.1b}$$

with the understanding that only linearly independent components of u_i and t_i can be prescribed at a point. The equation corresponding to the unprescribed component of u_i and t_i is written as $0 = 0$. Here \mathbf{n} is an outward unit normal to the boundary Γ . We write the boundary condition (2.4c₃) as

$$\mathbf{p}(\boldsymbol{\sigma}) = \mathbf{A}\boldsymbol{\sigma} = \mathbf{0} \quad \text{on } \Gamma_c, \tag{4.1c}$$

where

$$\mathbf{A} = \begin{bmatrix} 0 & \pm\mu_f & 1 \\ 0 & 0 & 0 \end{bmatrix}, \quad \boldsymbol{\sigma} = \begin{Bmatrix} \sigma_{11} \\ \sigma_{22} \\ \sigma_{12} \end{Bmatrix}, \quad (4.1d)$$

and $\Gamma_c = [0, L] \times \{\pm 1\}$. At points of Γ_c , the natural boundary condition (4.1b) is replaced by (4.1c).

Select a set of discrete points $\{\mathbf{x}_1, \mathbf{x}_2, \dots, \mathbf{x}_N\}$ in and on the boundary of Ω ; these points will henceforth be called nodes. For $\mathbf{x} \in \Omega$, let $\Omega_{\mathbf{x}} \subset \Omega$ be the neighborhood of \mathbf{x} , and \mathbf{v} be a test function defined on $\Omega_{\mathbf{x}}$. Taking the inner product of Eq. (2.1) with \mathbf{v} , of Eq. (4.1a) with $\alpha\mathbf{v}$, and of Eq. (4.1c) with $\beta\mathbf{v}$, integrating the resulting equations on $\Omega_{\mathbf{x}}$, $\Gamma_{\mathbf{x}} = \Gamma \cap \partial\Omega_{\mathbf{x}}$, and $\Gamma_{c\mathbf{x}} = \Gamma_c \cap \partial\Omega_{\mathbf{x}}$ respectively, adding them, and using the divergence theorem, we obtain

$$\int_{\Omega_{\mathbf{x}}} \sigma_{ij} v_{i,j} \, d\Omega + \int_{\Gamma_{\mathbf{x}}} \alpha v_i (u_i - \bar{u}_i) \, d\Gamma + \int_{\Gamma_{c\mathbf{x}}} \beta v_i p_i \, d\Gamma - \int_{\Gamma_{\mathbf{x}}} v_i t_i \, d\Gamma = 0. \quad (4.2)$$

Here α and β are scalar functions of \mathbf{x} defined on $\Gamma_{\mathbf{x}}$ and can be viewed either as Lagrange multipliers in which case they are to be determined as a part of the solution of the problem or as preassigned penalty parameters; their dimensions are such as to make Eq. (4.2) dimensionally correct. In order to obtain two sets of equations for the two components of \mathbf{u} , we select two linearly independent functions $\mathbf{v}^{(1)}$ and $\mathbf{v}^{(2)}$ in Eq. (4.2). The functions \mathbf{v} could be different for each node point; we signify this by writing $\mathbf{v} = \mathbf{v}(\mathbf{x}, \mathbf{x}_A)$.

In order to find an approximate solution, we replace $\mathbf{u}(\mathbf{x})$ by $\mathbf{u}^h(\mathbf{x})$ in Eq. (4.2) and set

$$u_i^h(\mathbf{x}) = \phi_A(\mathbf{x}) \hat{u}_{Ai} \quad (A = 1, 2, \dots, n; \quad i = 1, 2), \quad (4.3)$$

where $\phi_1(\mathbf{x}), \phi_2(\mathbf{x}), \dots, \phi_n(\mathbf{x})$ are linearly independent functions defined on $\hat{\Omega}_{\mathbf{x}}$, and \hat{u}_{Ai} are $2n$ scalar quantities which are not necessarily associated with the values of $\mathbf{u}^h(\mathbf{x})$ at any point $\mathbf{x} \in \Omega_{\mathbf{x}}$. We use the moving least squares method to ascertain functions $\phi_1(\mathbf{x}), \phi_2(\mathbf{x}), \dots, \phi_n(\mathbf{x})$. We refer the reader to [13] for details of finding the basis functions $\phi_i(\mathbf{x})$ and the definition of $\hat{\Omega}(\mathbf{x})$. However, we note that in a two-dimensional problem $\Omega(\mathbf{x})$ is usually a circle but $\hat{\Omega}(\mathbf{x})$ is an irregular shaped region.

Substituting for $\mathbf{u}^h(\mathbf{x})$ from (4.3) into (4.2) we arrive at two linear equations in $2n$ unknowns \hat{u}_{Ai} . Repeating this process for \mathbf{x} located at each one of the N nodes and assembling them, we arrive at the following system of $2N$ equations in $2N$ unknowns:

$$\mathbf{K}\mathbf{u}^h = \mathbf{f}, \quad (4.4)$$

where

$$\mathbf{K}_{LM} = \sum_{\mathbf{x}} \left[\int_{\Omega_{\mathbf{x}}} \boldsymbol{\varepsilon}_{\mathbf{v}}(\mathbf{x}, \mathbf{x}_L) \mathbf{D}\mathbf{B}_M \, d\Omega + \int_{\Gamma_{\mathbf{x}}} \alpha \mathbf{v}(\mathbf{x}, \mathbf{x}_L) \mathbf{S}\phi_M \, d\Gamma + \int_{\Gamma_{\mathbf{x}}} \mathbf{v}(\mathbf{x}, \mathbf{x}_L) \mathbf{N}\mathbf{D}\mathbf{B}_M \mathbf{S} \, d\Gamma + \int_{\Gamma_{c\mathbf{x}}} \beta \mathbf{v}(\mathbf{x}, \mathbf{x}_L) \mathbf{A}\mathbf{D}\mathbf{B}_M \, d\Gamma \right], \quad (4.5a)$$

$$\mathbf{f}_L = \sum_{\mathbf{x}} \left[\int_{\Gamma_{\mathbf{x}}} \mathbf{v}(\mathbf{x}, \mathbf{x}_L) \bar{\mathbf{t}} \, d\Gamma + \int_{\Gamma_{\mathbf{x}}} \alpha \mathbf{v}(\mathbf{x}, \mathbf{x}_L) \mathbf{S} \bar{\mathbf{u}} \, d\Gamma \right], \quad (4.5b)$$

$$\mathbf{N} = \begin{bmatrix} n_1 & 0 & n_2 \\ 0 & n_2 & n_1 \end{bmatrix}, \quad (4.5c)$$

$$\mathbf{B}_L = \begin{bmatrix} \phi_{L,1} & 0 \\ 0 & \phi_{L,2} \\ \phi_{L,2} & \phi_{L,1} \end{bmatrix}, \quad (4.5d)$$

$$\mathbf{D} = \begin{bmatrix} \lambda + \mu & \mu & 0 \\ \mu & \lambda + \mu & 0 \\ 0 & 0 & \mu \end{bmatrix}, \quad (4.5e)$$

$$\boldsymbol{\sigma}^T = [\sigma_{11} \quad \sigma_{22} \quad \sigma_{12}], \quad \boldsymbol{\varepsilon}^T = [\varepsilon_{11} \quad \varepsilon_{22} \quad 2\varepsilon_{12}], \quad (4.5f)$$

$$\mathbf{S} = \begin{bmatrix} s_1 & 0 \\ 0 & s_2 \end{bmatrix}, \quad s_i = \begin{cases} 1 & \text{if } u_i \text{ is prescribed on } \Gamma_{\mathbf{x}}, \\ 0 & \text{if } u_i \text{ is not prescribed on } \Gamma_{\mathbf{x}}. \end{cases} \quad (4.5g)$$

The approximate displacement field is computed from Eq. (4.3), and then strains and stresses can be evaluated at any point. In the solution of the problem we took α and β as penalty parameters and set their magnitudes equal to 10^8 .

5. Results

Both the numerical and the analytical solutions have been computed for $\nu = 0.25$, $u_0 = 1$, and for a broad range of values of the coefficient of friction, μ_f . The analytical solution is for a semi-infinite strip, and the numerical solution, unless otherwise specified, for $L = 15$. A regular mesh of 1089 nodes is used over the analysis domain. The roots of $h(p) = 0$ were found by using the bisection method for the real roots and Newton's method for the complex ones. The series were summed by retaining enough terms to ensure that $|s_{n+1} - s_n|/|s_n| < 0.001$ where s_n is the n th partial sum. It was found that there exists a critical value of the friction coefficient, $\mu_{f_{\text{crit}}} \cong 1.4$, that separates two distinct types of deformations of the elastic medium.

For subcritical μ_f , boundary condition (2.4c₃) applies and was verified a posteriori by the computed solution. A typical observation is that increasing μ_f magnifies the effect of friction without any qualitative change. Results for $\mu_f = 1$ are typical, and are discussed below.

Figs. 2(a) and (b) exhibit the variation of the horizontal displacement u_1 with the vertical coordinate x_2 for several values of x_1 , and the variation of u_1 with x_1 for five values of x_2 . On a cross-section (i.e. the plane $x_1 = \text{const.}$) the horizontal displacement is uniform except for slightly smaller values near the top and bottom walls. (Due to the symmetry of the problem about the horizontal centroidal axis, results for only the upper half of the strip are displayed.) However, the horizontal displacement decays quite rapidly in the x_1 -direction. These plots suggest that the horizontal displacement is greatest at the surface $x_1 = 0$, and for a fixed x_1 is greatest on the

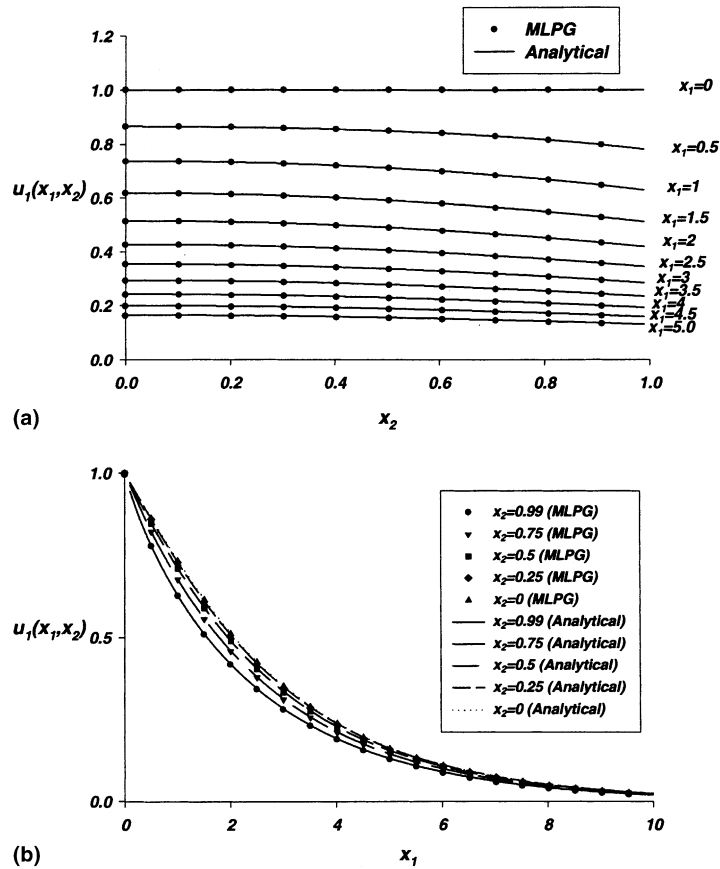


Fig. 2. (a) Variation of the horizontal displacement on several vertical planes; (b) variation of the axial displacement on several horizontal planes.

centerline $x_2 = 0$. Because $u_1(x_1, 0.99) > 0$, the frictional force on the top wall always acts in the negative x_1 -direction. An excellent agreement between the numerical and the analytical results implies that $L = 15$ is sufficient for computing numerical results with $\mu_f = 1$. Figs. 3(a) and (b) exhibit the through-the-thickness distribution of the vertical displacement, u_2 , for several values of x_1 , and the variation of u_2 along the domain length, x_1 , with x_2 fixed. It is clear that the vertical displacement also decays in the x_1 -direction. Observe that $u_2(x_1, x_2)$ is negative for small x_1 but positive for large x_1 . Thus the material moves towards the centerline of the strip near the left edge but towards the top and the bottom walls in the interior. The maximum value of $|u_2(x_1, x_2)|$ is of the order of 10^{-2} whereas that of $|u_1(x_1, x_2)|$ is 1.

Figs. 4(a)–(c) depict the variation on different horizontal planes of the stresses σ_{11} , σ_{22} and σ_{12} scaled by the Lamé constant λ . Note that all of the stresses decay to zero with an increase in x_1 . All three stress components change rapidly in the x_1 -direction near the corner $x_1 = 0$, $x_2 = 1$. Recall that the conclusion from the corner analysis was that there were no solutions of the field equations with regular displacements and singular but integrable stress fields. However, there may be solutions in which the second derivatives of the displacement are unbounded as the corner is

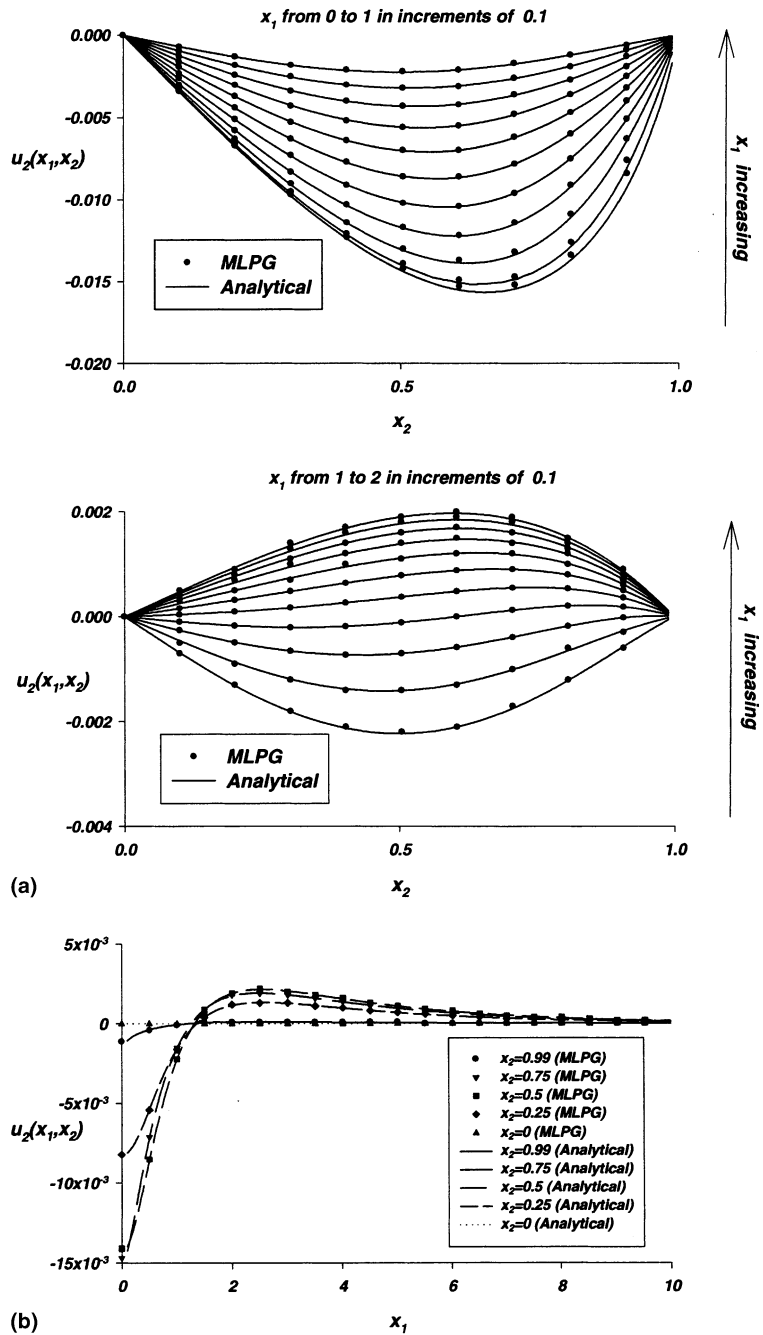


Fig. 3. (a) Through-the-thickness distribution of the vertical displacement on several vertical planes; (b) variation of the vertical displacement on several horizontal planes.

approached. Thus the stresses are bounded at the corner but may have infinite slopes. Note that $\sigma_{12}(0, 1) = 0$ is required by the boundary condition (2.4b)₂. Thus $\sigma_{12}(x_1, 1)$ increases rapidly from 0 at $x_1 = 0$ to a finite value a short distance away from the edge $x_1 = 0$. The variation of σ_{11} and

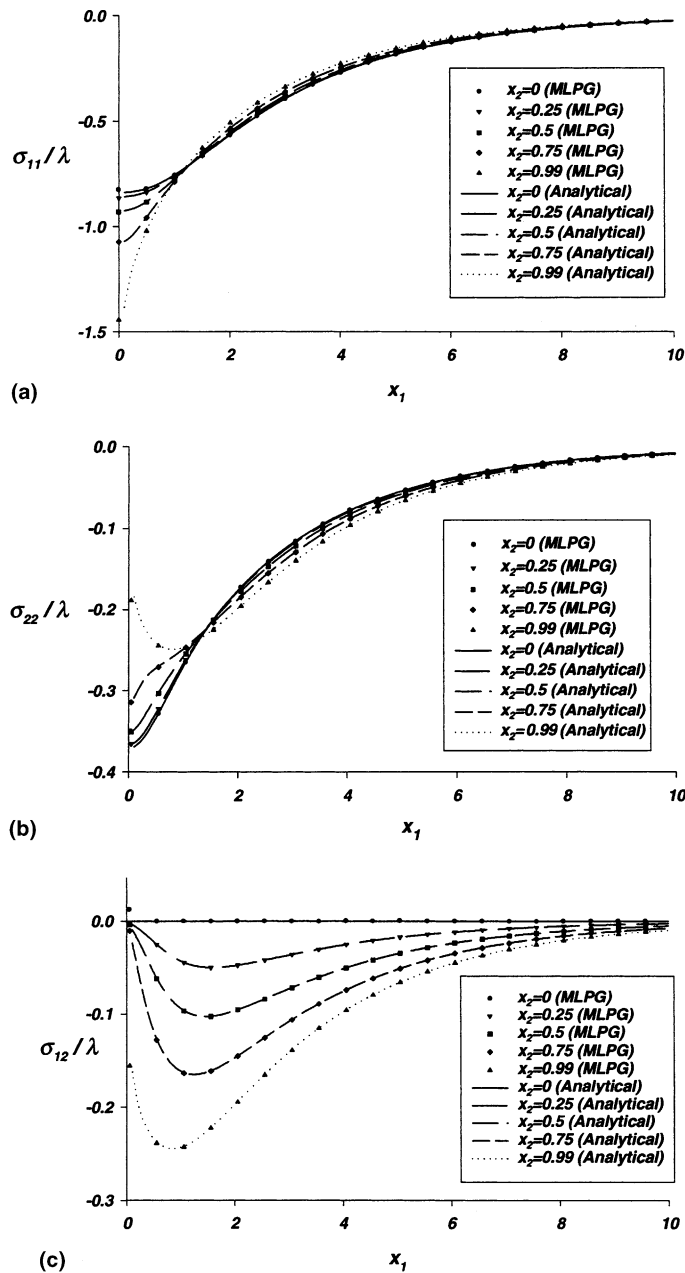


Fig. 4. (a) Variation of the normalized axial stress on several horizontal planes; (b) variation of the normalized transverse normal stress on several horizontal planes; (c) variation of the normalized shear stress on several horizontal planes.

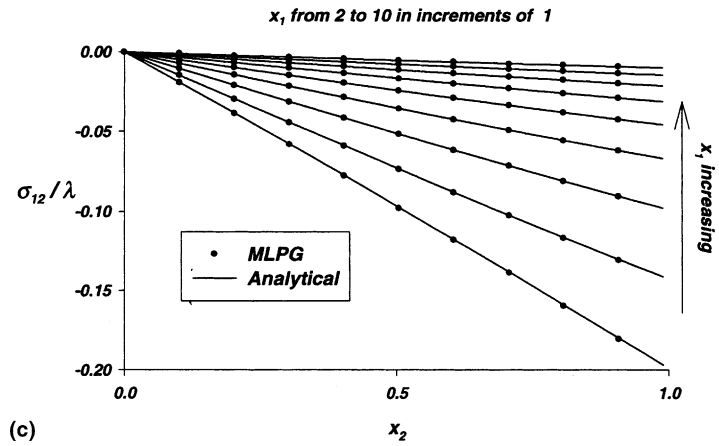
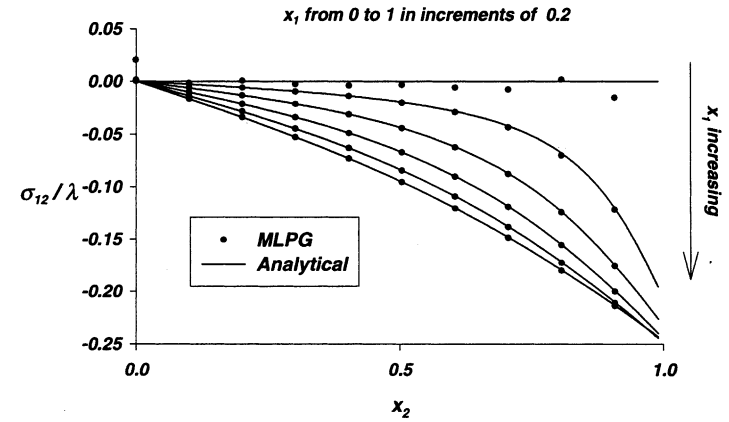
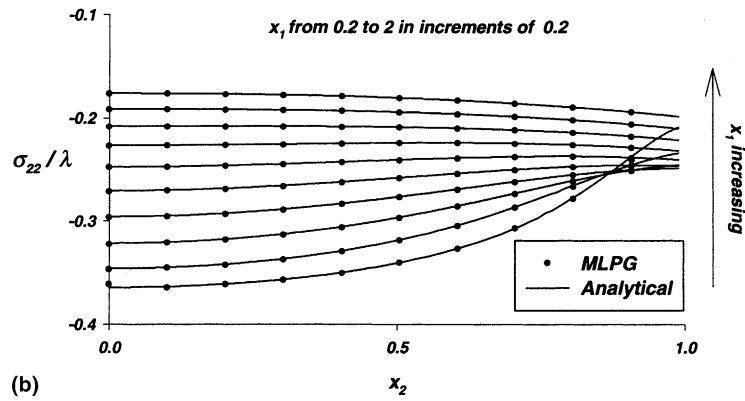
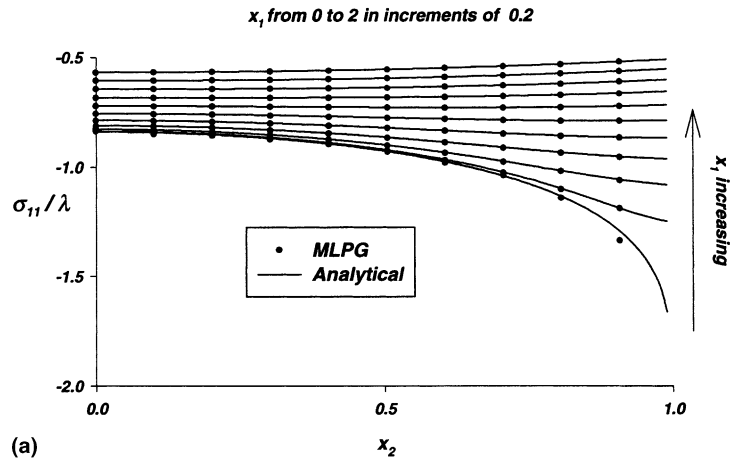


Fig. 5. (a) Through-the-thickness distribution of the normalized axial stress on several vertical planes; (b) through-the-thickness distribution of the normalized transverse normal stress on several vertical planes; (c) through-the-thickness distribution of the normalized shear stress on several vertical planes.

σ_{22} at the corner in the x_1 -direction is also quite sharp. Since $\sigma_{11}/\lambda = O(1)$, the presumed value of $u_0 = 1$ is too large and the computed solution is outside the range of validity of the linear theory. Because the problem being studied is linear, the qualitative nature of the solution is preserved and the magnitude of the computed displacements and stresses will scale down linearly with a change in the value of u_0 .

From the variation of stresses on several vertical planes plotted in Figs. 5(a)–(d), it is evident that through-the-thickness distributions of σ_{11} and σ_{22} on vertical planes $x_1 \geq 1.0$ are nearly uniform. However, on the plane $x_1 = 0$, σ_{11} varies sharply near the top wall and the same holds for σ_{22} on vertical planes $x_1 = 0.2$ and 0.4 . The shear stress σ_{12} essentially vanishes on the vertical plane $x_1 = 10$, varies nearly linearly on vertical planes $1 \leq x_1 \leq 9$, and rapidly on the vertical planes $0.2 \leq x_1 \leq 0.8$. In order to see if the differences between the values of σ_{12} on the left edge computed from the numerical and the analytical solutions were caused by the discretization of the domain, we refined the nodal mesh. Results from the refined mesh are exhibited in Fig. 6 and show that $\sigma_{12}(0, 0) = 0$ is well satisfied, and that σ_{12} exhibits a boundary-layer effect near the top wall. The boundary condition $\sigma_{12}(0, 1) = 0$ at the corner is not satisfied even for the finer mesh. It is due to

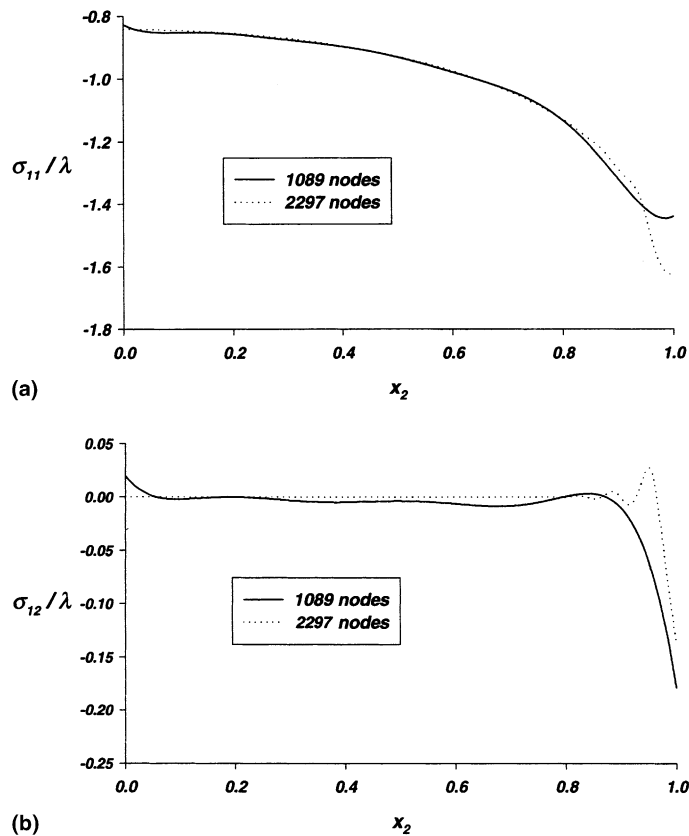


Fig. 6. (a) Comparison of through-the-thickness distribution of the normalized axial stress on the left edge computed with two nodal meshes; (b) comparison of through-the-thickness distribution of the normalized shear stress on the left edge computed with two nodal meshes.

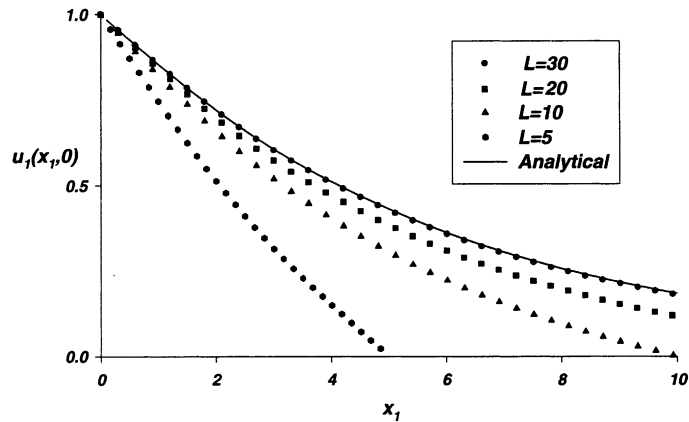


Fig. 7. Variation of the axial displacement on the centerline for four lengths of the domain.

the conflicting requirements at the corner since the boundary condition (2.4c₃) necessitates that $\sigma_{12}(0, 1) \neq 0$ for the material point to stay in contact with the wall, unless $\sigma_{22}(0, 1) = 0$.

Fig. 7 displays the variation of $u_1(x_1, 0)$ on the centerline of the strip for four different values of the domain length L and the coefficient of friction, $\mu_f = 0.5$. It is clear that the decay rate of $u_1(x_1, 0)$ near the left edge is unaffected by increasing L from 15 to 30 but the decay rate of $u_1(x_1, 0)$ away from the left edge is slower for $L = 30$ as compared to that for $L = 15$. However, the decay rate of $u_1(x_1, 0)$ near the left edge increases noticeably as L is decreased from 10 to 5. Within the region $0 \leq x_1 \leq 1.5$ where sharp variations in σ_{11} , σ_{22} and σ_{12} occur, the two solutions computed with $L = 15$ and 30 are virtually identical.

Solutions for other values of μ_f between 0 and 1.4 reveal that the qualitative behaviors of the displacements and the stresses are unaffected by the value of μ_f but the rate of decay of the solution in the x_1 direction changes with μ_f . The horizontal displacements on the centerline plotted in Fig. 8(a) for $\mu_f = 0.5$, 1.0 and 1.4 reveal that their decay rate increases with an increase in the value of μ_f . The discrepancy between the analytically and the numerically computed values of σ_{22} at the point (1, 0.99) (cf. Fig. 8(b)) for $\mu_f = 0.1$ disappears when the length of the domain is increased (cf. Fig. 7) from 15 to 30. The values of σ_{12} at the point (1, 0.99) computed from the numerical solution for the four values of μ_f agree well with their respective analytical values. Fig. 9 displays the axial location x_1^* at which the analytical value of $u_1(x_1^*, 0) = 0.01$ or 1% of its value at $x_1 = 0$. It suggests that the solution for the infinite strip provides a good approximation to the solution for the finite strip provided that it is long enough. On each vertical plane, the magnitude of the three stresses at a point adjacent to the top wall increases with an increase in the magnitude of μ_f ; this is illustrated in Figs. 8(b) and (c) wherein σ_{12} and σ_{22} at the point (1, 0.99) vs. μ_f are plotted.

For values of the coefficient of friction $\mu_f > 1.4$, the deformations of the material points are quite different from those for $\mu_f < 1.4$. This is seen readily by examining Figs. 10(a) and (b), which are for $\mu_f = 5.0$ and display the variation of the horizontal displacement u_1 and the normalized shear stress on three horizontal planes. While the magnitudes of these quantities continue to decay with x_1 , the profiles are no longer monotonic but oscillatory, with both the axial displacement and the shear stress taking on positive as well as negative values. In order to understand the mathematical origin

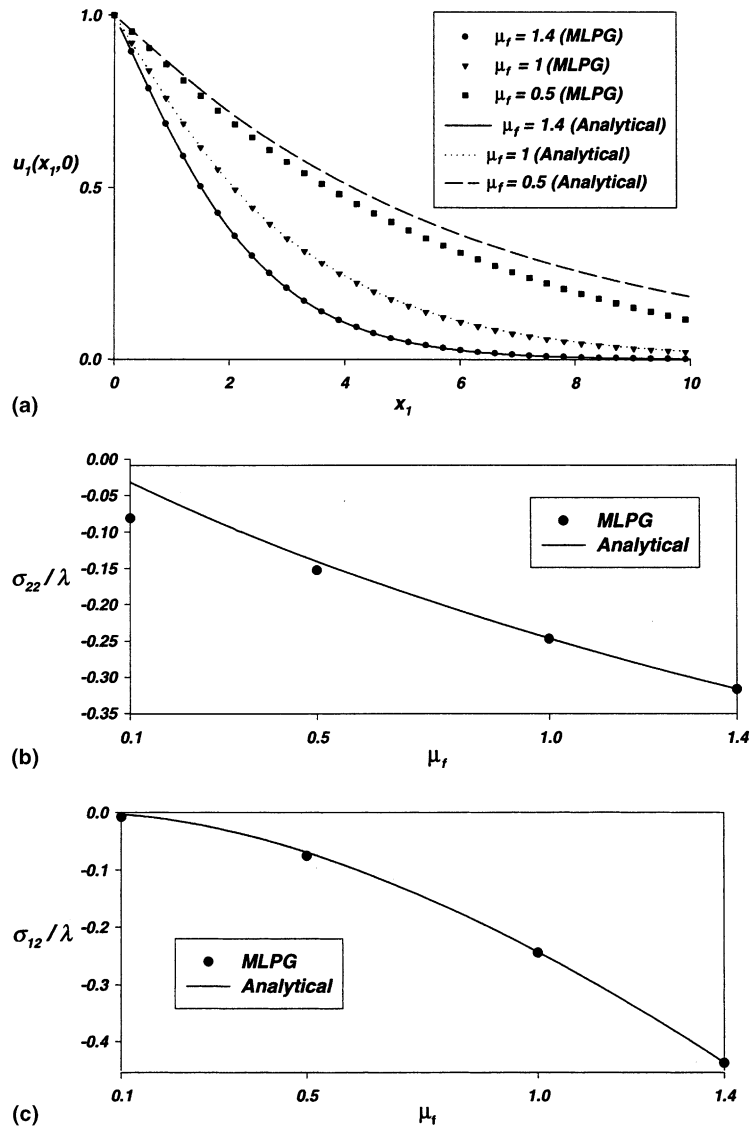


Fig. 8. (a) Variation of the axial displacement on the centerline for three values of μ_f ; (b) variation with μ_f of the normalized transverse normal stress at the point (1, 0.99) on the top wall; (c) variation with μ_f of the normalized shear stress at the point (1, 0.99) on the top wall.

of this behavior, we recall that away from $x_1 = 0$, the character of the solution is determined predominantly by those poles in the transform plane that are closest to the imaginary axis. The location of the first six poles as a function of μ_f is exhibited in Figs. 11(a)–(c). Figs. 11(a) and (b) depict, respectively, the dependence of the real and the imaginary parts of the pole locations on μ_f , while Fig. 11(c) shows the locations of the poles in the complex plane for a number of values of μ_f . The rightmost pair of poles are both real for small enough μ_f . As μ_f increases, one pole moves towards the origin while the other moves away from it until they meet and become a complex

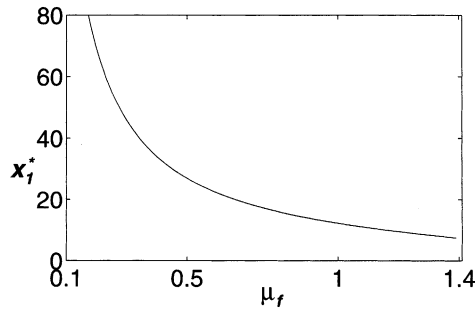


Fig. 9. Value of x_1^* at which $u_1(x_1^*, 0) = 0.01 u_1(0, 0)$ versus μ_f .

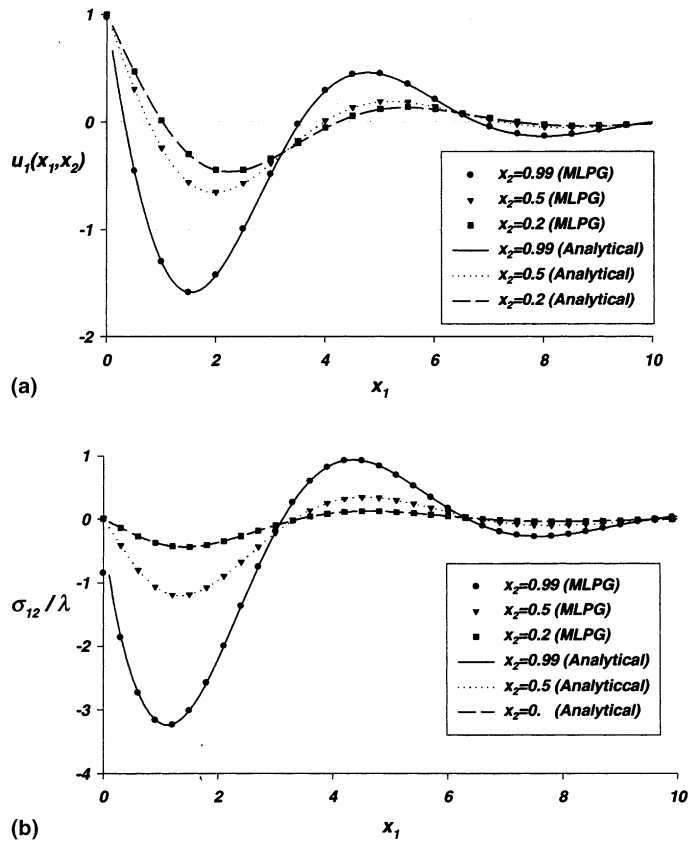


Fig. 10. (a) and (b) For $\mu_f = 5$, variation of the axial displacement and the normalized shear stress on three horizontal planes.

conjugate pair. The real part of this complex conjugate pair then decreases with an increase in μ_f while the imaginary part increases. This behavior is also seen in each successive pair of poles, however the value of μ_f at which two real poles change into a complex pair is smaller for the poles with more negative real parts. Recalling that the solution has the form $\sum_{p_k} e^{p_k x_1} f(p_k, x_2)$, at the

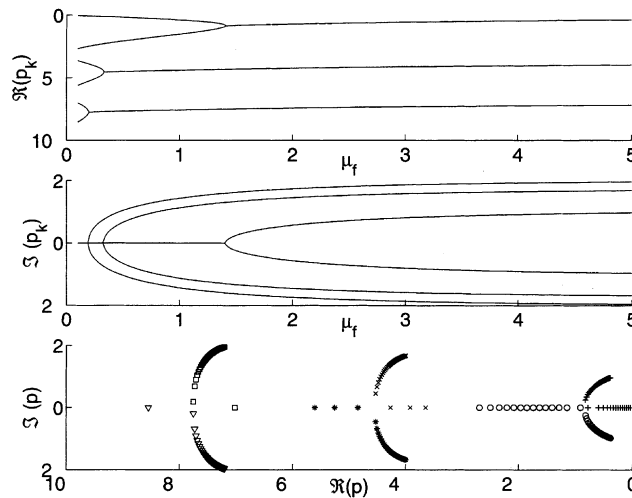


Fig. 11. Dependence of the pole locations on μ_f .

critical value of $\mu_f \cong 1.4$, the two largest terms in the expansion make the transition from having an exponential decay in x_1 to having a sinusoidal behavior with exponentially decaying amplitude. Furthermore, an increase in μ_f decreases the amplitude of the exponential decay and the oscillations become more pronounced.

6. Conclusions

We have analyzed plane-strain static deformations of a homogeneous, isotropic, linear elastic body enclosed within a rigid rectangular cavity with rough side walls but a smooth right end. The material is compressed by prescribing uniform axial displacements at the left end. The problem is solved both analytically by the Laplace transform technique and numerically by the moving least squares Petrov–Galerkin method which requires only the locations of the nodes. The analytical solution is for an infinite length of the cavity and the numerical solution is for the finite cavity. Coulomb’s friction law is assumed to apply at the two rigid walls.

It is found that there is a critical value of the coefficient of friction, $\mu_{f,crit} \cong 1.4$. For $\mu_f < \mu_{f,crit}$, the axial displacements of points decay monotonically with distance from the left edge and the material points stay in contact with the rough walls. Also, the rate of decay of the solution variables in the axial direction increases with an increase in the value of μ_f . The analytical solution for the infinite cavity represents well the deformations of the material compressed in the finite cavity for larger values of μ_f .

For $\mu_f > \mu_{f,crit}$, axial displacements and stresses on the rough walls exhibit oscillatory behavior in the axial direction, with the amplitude of oscillations decaying with increasing axial distance from the left end. The shear stress undergoes changes in sign and the material separates from the walls, so that the analytical solution presented here can no longer be deemed physically relevant. The situation is analogous to what had been observed in the earlier study on powders sliding in rough tubes [1], which had motivated the present investigation. The implication is that at high

levels of roughness the Coulomb friction model is no longer adequate, as it fails to capture faithfully the complex interaction between the now larger asperities and imperfections in the sliding surfaces. It is possible that the boundary conditions (2.4c₂)–(2.4c₄) then apply on different (and a priori unknown) segments of the walls, but that is a difficult problem which we have not examined.

Acknowledgements

Partial support for this work was provided by the National Science Foundation.

References

- [1] L.G. Hill, A.K. Kapila, Dynamic compaction of granular materials in a tube with wall friction, applied to DDT, in: B. Sturtevant, J.E. Shepherd, H.G. Hornung (Eds.), *Proceedings of the 20th International Symposium on Shock Waves*, World Scientific, Singapore, 1995, pp. 1413–1418.
- [2] A.W. Warlock, Effect of wall friction on compaction and compression, Ph.D. Thesis, Rensselaer Polytechnic Institute, 1997.
- [3] W.L. Elban, M.A. Chiarito, The strain-rate behavior of coarse HMX porous bed compaction, *Powder Technol.* 46 (1986) 181–187.
- [4] J.M. McAfee, B.W. Asay, A.W. Campbell, Deflagration to detonation transition in granular HMX, in: *Proceedings of the Ninth Symposium (International) on Detonations*, Portland, OR, 1989, pp. 265–278.
- [5] N.I. Muskhelishvili, *Some Basic Problems of the Mathematical Theory of Elasticity*, Noordhoff, Leiden, 1963.
- [6] R.C.T. Smith, The bending of a semi-infinite strip, *Aust. J. Sci. Res.* 5 (1952) 227–237.
- [7] M.W. Johnson Jr., R.W. Little, The semi-infinite elastic strip, *Quart. Appl. Math.* 22 (1965) 335–344.
- [8] R.D. Gregory, The traction boundary-value problem for the elastic semi-infinite strip, existence of solutions and completeness of the Papkovitch–Fadle eigen functions, *J. Elasticity* 10 (1980) 295–327.
- [9] D.D. Joseph, The convergence of biorthogonal series for biharmonic and Stokes flow edge problems, *SIAM J. Appl. Math.* 33 (1977) 337–347.
- [10] D.A. Spence, A note on the eigenfunction expansions for the elastic strip, *SIAM J. Appl. Math.* 42 (1982) 155–173.
- [11] R.D. Gregory, I.J. Gladwell, The cantilever beam under tension, bending or flexure at infinity, *J. Elasticity* 12 (1982) 317–343.
- [12] D.C. Champeney, *A Handbook of Fourier Theorems*, Cambridge University Press, Cambridge, 1987.
- [13] S.N. Atluri, T. Zhu, A new meshless local Petrov–Galerkin (MLPG) approach in computational mechanics, *Comput. Mech.* 22 (1998) 117–127.